Mixed layer thermodynamics of the Southern South China Sea

Bijoy Thompson · Pavel Tkalich

Abstract Seasonal and inter-annual variability of the mixed layer temperature in the Southern South China Sea (SSCS) is investigated using a regional ocean circulation model simulation. The mixed layer depth (MLD) over the SSCS exhibits a strong seasonal signal with deeper MLDs during the northeast and southwest monsoons. The main factor that drives the mixed layer temperature variation in the SSCS is the air-sea heat fluxes, with vertical ocean processes acting as a relatively weak negative feedback. In general, the budget analysis demonstrates a net balance between the vertical ocean processes and surface heat flux during the pre-monsoon and southwest monsoon. Northeast monsoon period is noted by an offsetting of surface heat flux, horizontal and vertical ocean processes. The first dominant mode of mixed layer temperature inter-annual variability in the SSCS shows significant correlation (0.34) with the El Nino phenomenon in the Pacific Ocean and is best correlated (0.67) with a lag of 5 months.

**Keywords** South China Sea · ROMS · Mixed layer · Heat budget

1 Introduction

The South China Sea (SCS) is the largest marginal sea in the western Pacific Ocean, connected with the Pacific Ocean by the deep Luzon Strait in the northeast, in the west with the Andaman Sea through the Malacca Strait and in the south with the Java Sea through the Karimata Strait

B. Thompson (✉) · P. Tkalich
Tropical Marine Science Institute, National University
of Singapore, Singapore 119222, Singapore
e-mail: bijoymet@gmail.com

(Fig. 1). Subjected to the influence of the Asian monsoon, the SCS exhibits pronounced seasonal variability (Wyrtki 1961; Chu et al. 1997; Wu et al. 1998; Qu 2001). The inter-annual and long-term variability of the SCS upper ocean circulation (Wu et al. 1998; Klein et al. 1999; Chu et al. 1999; Qu 2000; Fang et al. 2005; Wang et al. 2006a; Rong et al. 2007; Liu et al. 2008, 2011; Yang and Wu 2012), sea surface temperature (SST) (Fang et al. 2006; Kienast et al. 2001; Wang et al. 2002; Xie et al. 2003; Liu et al. 2004, 2007, 2009; Cai et al. 2011), sea surface height (Ho et al. 2000; Li et al. 2002; Fang et al. 2006), and salinity (Liu et al. 2007) have been explored by several authors.

The El Nino-Southern Oscillation (ENSO) represents one of the major sources for Earth's climate variability. Dominant mode of the SST inter-annual variability in the Indian Ocean and SCS are related to the ENSO in the Pacific Ocean. Air-sea heat fluxes in the SCS are influenced by the ENSO events through atmospheric tele-connections (Klein et al. 1999; Wang et al. 2006b). Inter-annual variability of the SCS SST exhibits strong correspondence with the ENSO (e.g., Ose et al. 1997; Wang et al. 2002; Xie et al. 2003). As El Nino develops in the Pacific Ocean, the East-Asian northeast monsoon becomes weak (e.g., Tomita and Yasunari 1996), resulting in a reduced circulation in the SCS (Chao et al. 1996; Wu et al. 1998). In response to the monsoon circulation anomalies, SST increases over much of the SCS and peaks in the following southwest monsoon period (Xie et al. 2003). The SCS mixed layer dynamics has a significant role in modulating the SST during the ENSO events (Wang et al. 2000, 2006a). Fang et al. (2006) showed that from 1993 to 2003 the first dominant mode of SST variability over the SCS has highest correlation with the Nino3.4 index when the lag is 8 months. Analysis by Klein et al. (1999) revealed that the SST anomaly over the SCS, from 1952 to 1992, is best

Fig. 1 The South China Sea with major passages of water mass transport with the Pacific and Indian Oceans. The *middle box* represents the SSCS model domain. The eastern equatorial Indian Ocean is masked in our SSCS model configuration. The *inner box* indicates the regions where the model simulation is used for the EOF and heat budget analysis. *Shading* represents the bathymetry in meters
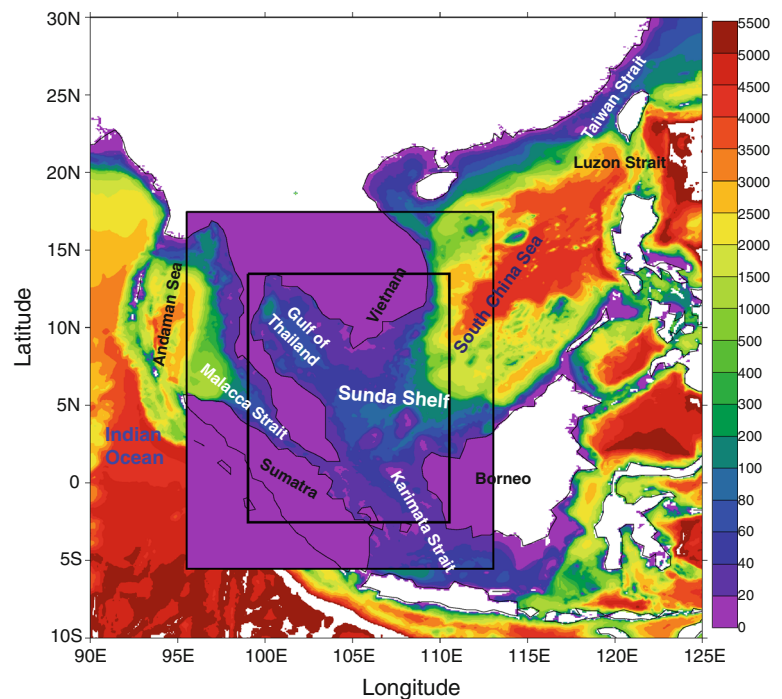
correlated to the ENSO index with a 5-month lag. Delayed appearance of the ENSO-induced SST anomalies in remote ocean basins has been investigated in earlier studies (e.g., Lau and Nath 1996; Klein et al. 1999; Alexander et al. 2002). The mechanisms suggested to explain the influences of tropical Pacific SST anomalies on remote oceans is the "Atmospheric Bridge" and thermal inertia of the ocean. Klein et al. (1999) suggested that the atmospheric circulation anomalies associated with the ENSO induce changes in the regions of convection and cloud cover, which alters the air-sea heat fluxes over the remote ocean basins.

The air-sea coupled phenomena characterized by opposite temperature anomalies in the southeastern tropical Indian Ocean and western equatorial Indian Ocean is known as the Indian Ocean Dipole (IOD)/zonal mode (Saji et al. 1999; Webster et al. 1999). Influences of IOD on regional and global climate variability are addressed in many studies (e.g., Saji and Yamagata 2003). Yuan et al. (2008) investigated the impact of IOD on the Asian summer monsoon in the year following the IOD event, including the Southeast Asian region. A study by Fang et al. (2006) showed that the second dominant mode of surface wind and wind stress variability over the SCS is significantly correlated with the IOD.

The Southern South China Sea (SSCS) comprises one of the largest sea-shelves called the Sunda Shelf, with a width of about 700 km extending from the eastern coast of Peninsular Malaysia to the eastern edge of the SCS (Fig. 1). Depth of water in the Sunda Shelf varies from 40 to 100 m while moving from the south to central part of the

SCS. The Malacca Strait consists of a wide and deep (depth of 100 m) section contracting from the Andaman Sea to the south (north section) as well as a narrow (27 km) and shallow (depth around 30 m) south section. Most of the earlier studies on SCS addressed the seasonal or long-term variability in the deep or northern basins. Scarcity of observations or relatively coarse resolutions of the numerical models have restricted earlier studies from focusing on examining the upper ocean thermal structure in the southern SCS region. Qu (2001) demonstrated that the SCS exhibits distinct thermodynamical characteristics in the continental slopes of China, off west Luzon, central SCS and near the Vietnam coast. Qu et al. (2005) suggested that the SST over the SSCS and Indonesian region is of major importance to the atmospheric state from regional to global scales. Since the SSCS and Indonesian seas lie alongside the equator, the region is recognized as a primary energy source for the global circulation system. In addition, this region is situated in the middle of the Indo-Pacific warm pool, where frequent convective storms contribute to the ascending branch of the equatorial Pacific Ocean Walker circulation. Consequently, the upper ocean thermal structure of the SSCS has a vital role in determining/ altering the air-sea interaction over the region (Qu et al. 2005).

The vertically averaged temperature over the ocean surface mixed layer has been widely used as a proxy for the SST (e.g., Kim et al. 2006; de Boyer Montegnt et al. 2007; Grodsky et al. 2008). The mixed layer is often characterized by strong vertical mixing and very weak stratification.

The effects due to the intense vertical mixing within the mixed layer can be avoided by employing the mixed layer temperature as an alternative to the SST (Kim et al. 2006). Since the mixed layer interacts with the atmosphere and the interior of the ocean, the mixed layer temperature has a vital role in determining the atmospheric and ocean circulation. Motivated by the results from Qu (2001), the main objective of this study is to present a comprehensive analysis of the seasonal and inter-annual variability of the mixed layer temperature and ocean dynamic processes in the SSCS region. The role of the ENSO on the mixed layer temperature variability in the region is also explored in this study. Model study by Qu et al. (2004) suggested that the Luzon Strait transport has an important role in conveying the effect of the ENSO to the SCS. Their study revealed that the Luzon Strait transport is generally stronger during the El Nino and weaker during the La Nina events. In this context, the significance of horizontal water mass advection during the ENSO events on the SSCS mixed layer temperature variation is examined. Identifying the local and remote influences on the mixed layer thermodynamics will be useful in understanding the SST and upper ocean temperature variability in the SSCS.

Here we use a regional ocean circulation model, forced by inter-annually varying surface and lateral boundary conditions, configured for the SSCS-Malacca Strait region to address the upper ocean thermodynamical characteristics. Our diagnostics of the ocean model results are aimed at examining the spatio-temporal variation of the mixed layer ocean properties in the SSCS. First, a brief discussion on the ability of model to reproduce the climatological features in SST, surface circulation, and sea surface height anomaly (SSHA) over the SSCS, and a comparison of model surface fields against satellite observations is presented. The relationship between mixed layer depth (MLD) and SST in the SSCS is then investigated. Heat budget analysis has been performed to recognize the relative importance of ocean dynamics and air-sea fluxes in driving the mixed layer temperature seasonal variation in the region. The dominant modes of mixed layer temperature inter-annual variability in the SSCS are identified using the empirical orthogonal function (EOF) analysis. Further, the possible interactions between the leading EOF modes and the ENSO are also investigated.

2 Model configuration and datasets

The IRD (Institut de Recherches pour le Developpement) version of the regional ocean modeling system (ROMS) is used in the present study (Penven et al. 2006; Debreu et al. 2012). ROMS is a 3-dimensional, free-surface, primitive equation model based on hydrostatic vertical momentum balance and Boussinesq approximations. The model has stretched, terrain-following coordinates in the vertical, and curvilinear coordinates in the horizontal. Lateral tracer and momentum advection in the model is associated with the third-order upstream-biased scheme (Shchepetkin and McWilliams 1998). In tracer advection, the diffusion part is rotated along isopycnal surfaces to avoid spurious diapycnal mixing and loss of water masses (Marchesiello et al. 2009; Lemarié et al. 2012). Large-McWilliams-Doney K-profile planetary (KPP) boundary layer scheme is used for vertical mixing, which has both local and non-local mixings (Large et al. 1994).

The model domain extends from 95.5°E to 113°E in the x-direction and 5.5°S to 17.5°N in the y-direction with a uniform horizontal resolution of $1/16° \times 1/16°$ (Fig. 1). There are 32 vertical σ-levels and the upper mixed layer is well resolved (minimum 12 levels in the upper 100 m). The model bathymetry is derived from the general bathymetric chart of the oceans (GEBCO) database (http://www.gebco.net/) with 30 arc-second resolution. Model bathymetry is smoothed to reduce the pressure gradient errors and minimum water depth is set to 15 m. Open boundary conditions are prescribed in the lateral boundaries where an active, implicit, upstream-biased, radiation condition is implemented (Marchesiello et al. 2001); this connects the model solution to the simple ocean data assimilation (SODA) v2.0.2-4 re-analysis datasets (Carton and Giese 2008). Temperature, salinity, sea surface height, and baroclinic and barotropic velocities are supplied along the lateral open boundaries. The model has been integrated from 1990–2007 with the initial conditions from SODA for January 1990. Model simulations from 1991 to 2007 are used for detailed analysis in this study. The model is forced by 12-hourly 10-m wind, 2-m air temperature, relative humidity, downward shortwave and longwave radiations at the earth surface, and precipitation fields from European Centre for Medium-Range Weather Forecasts Re-Analysis (ERA)-interim dataset (Dee et al. 2011). The ocean surface heat fluxes are computed using the model SST, based on the bulk flux formulation by Fairall et al. (1996).

To compare the model simulated climatological and inter-annual SST and SSHA, SST derived from National Oceanic and Atmospheric Administration Advanced Very High Resolution (AVHRR) pathfinder infrared radiometer and SSHA derived from TOPEX/POSEIDON (T/P) satellite altimeter are used. AVHRR satellite series provide an unbroken SST observation from the same class of sensors over a period of about 25 years since 1985. Monthly AVHRR-pathfinder version 5 SST observation obtained from http://poet.jpl.nasa.gov for the period 1990–2007 is utilized in the analysis. The SSHA data provided by http://www.aviso.oceanobs.com is used in the analysis. The monthly SSHA climatology computed for the period 1993–2008 is compared with the model SSHA.

2.1 Methodology

The MLD is computed based on a variable density criterion. Here, the MLD is defined as the depth where the density increases corresponding to a temperature decrease of 0.5 °C from the surface.

The wind-forcing influences the behavior of the oceans mainly through the transfer of momentum flux, controlling the turbulent heat fluxes (latent and sensible heat fluxes), and through the production of turbulent kinetic energy near the ocean surface (Niiler 1975; Cushman-Roisin 1981; Pickard and Emery 1990). In the case of wind-driven circulations, the potential energy and mechanical energy increase required for the MLD deepening is supplied by the winds as turbulent kinetic energy. Using a turbulent erosion model, Cushman-Roisin (1981) demonstrated that the rate of change of potential energy as a result of mixing equals the turbulent kinetic energy input by wind at the fluid surface. After Niiler (1975), Qu (2001) suggested that the rate of wind stirring responsible for the MLD deepening can be expressed as wind kinetic energy (WKE):

$$Frictional\ Velocity,\ u_* = \sqrt{\tau/\rho},$$
$$Wind\ Kinetic\ Energy = \frac{1}{2} \cdot \rho \cdot u_*^3. \tag{1}$$

where τ is the surface wind stress and $\rho = 1{,}025$ kg/m^3, is the density of sea water.

The mixed layer heat budget of the SSCS is estimated based on the formulation described in Vialard and Delecluse (1998). Model temperature tendency terms averaged over the time-varying mixed layer are applied to estimate the proxies of physical tendencies in this method (Vialard et al. 2001). The model mixed layer temperature tendency is given as:

$$Temperature\ Tendency,$$
$$\partial_t T_{mld} = [Q_{flx}] + [Q_{hadv}] + [Q_{vertical}] + R$$
$$\partial_t T_{mld} = \left[\frac{(Q* + Q_S (1 - f_{(h)}))}{\rho\ C_p\ h} \right]$$
$$- \left[\frac{1}{h} \left(\int_0^h u \cdot \partial_x T_{mld} \cdot dz + \int_0^h v \cdot \partial_y T_{mld} \cdot dz \right) \right]$$
$$+ \left[\frac{1}{h}\left(\frac{dh}{dt} + w_{(h)} \right)\ \left(T_{mld} - T_{(h)} \right) + \frac{(K\,\partial_z T)_{(h)}}{h} \right]$$
$$+ R, \tag{2}$$

where, $h \sim$ mixed layer depth, Q^* and $Q_s \sim$ Non solar and solar components of heat flux, $Q_{vertical} =$ Sum of the vertical advection and vertical diffusion, $T \sim$ water temperature, $T_{mld} \sim$ mixed layer temperature, $T_h \sim$ Temperature at the bottom of mixed layer, $w_{(h)} \sim$ Vertical velocity at the bottom of mixed layer, $K \sim$ Vertical diffusion

coefficient, $C_p = 4{,}000$ J/kg/K, is the specific heat capacity of sea water, $R \sim$ Residual term for the unaccounted effects and fraction of shortwave flux reaches the depth, $f_{(h)} = Re^{-(h/l_1)} + (1 - R)e^{-(h/l_2)}$. Here, the attunation coefficients are selected for a Type I water (Jerlov 1968), $R = 0.58$, $l_1 = 0.35$ m, and $l_2 = 23$ m.

Heat content (HC) of the MLD is defined as:

$$HC_{(mld)} = \rho \int_{z=0}^{z=MLD} C_p \cdot T \cdot dz. \tag{3}$$

The ocean heat transport through the boundaries to the control volume is estimated as:

$$Heat\ Transport = \rho\ C_p \int_A T \cdot v_n \cdot dA.$$

Here, dA represents the area of the element and v_n is the velocity component perpendicular to the boundary.

3 Results

3.1 Model sea surface temperature

SST in situ observations are relatively sparse over the SSCS compared with the eastern Indian Ocean and western Pacific Ocean. Alternatively, satellite observations provide a reliable estimate of the ocean surface parameters to assess the accuracy of model simulation. The model simulated SST is compared with the AVHRR-Pathfinder SST observations for the study period from 1991 to 2007 as shown in Fig. 2. The monsoons have a dominant influence on the SST variation in the SSCS. The climatological evolution of SST in the SSCS from model and satellite observation demonstrates a bi-modal distribution with a prominent peak in May and a secondary peak in October. SST warming during the pre-monsoon (February–May) and inter-monsoon (October) periods and SST cooling in the southwest monsoon (June–September) and northeast monsoon (November–January) are well reproduced by the model and show good agreement with the observation. However, SST cooling in the SSCS during the northeast monsoon is slightly underestimated by the model (SST differences with the observation is less than 0.2 °C). The key features in the spatial SST distribution over this region, such as the upwelling and eastward advection of cold water off the Vietnam coast during the southwest monsoon and southward advection of cold water in the northeast monsoon (Wyrtki 1961; Qu 2001; Qu et al. 2005) are well reproduced by the model (figures not shown). During the pre-monsoon warming phase, the SSTs above 30 °C is observed in the Gulf of Thailand, Andaman

Sea-Malacca Strait and near equatorial regions of the model domain.

Correlation between the model SST and observation is significant above 99 % (correlation, $\gamma > 0.2$) in the SSCS
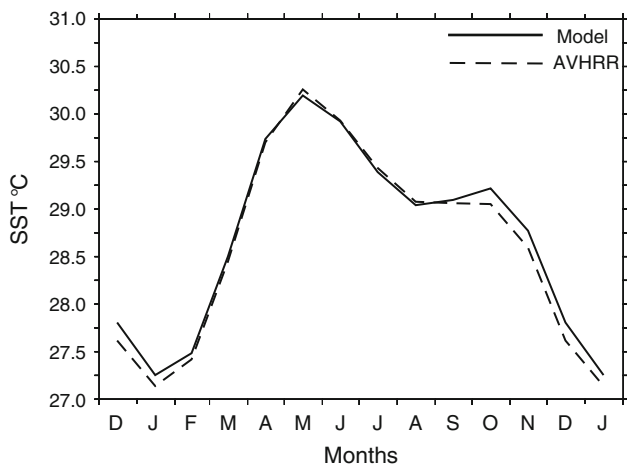

Fig. 2 Climatological evolution of SST in the SSCS from model (*black line*) and AVHRR-Pathfinder satellite observation (*dashed line*)

(Fig. 3a). Relatively low correlation is observed near the west coast of Borneo and in northern entrance of the Malacca Strait. Root mean square (RMS) difference between the model and observed SST is shown in Fig. 3b. RMS difference above 0.8 °C is seen along the coast of Vietnam and Borneo. A visual comparison of climatological SST suggests that the northward or southward advection of cold water along the Vietnam coast during the southwest or northeast monsoons is somewhat underestimated in the model simulation (figures are omitted). Also, standard deviation of the model SST is relatively weaker in the regions where the correlation is low or with higher RMS differences (Fig. 3c and d). The standard deviation of SST over the study region is less than 2.5 °C during 1990–2007. The amplitude of SST variation is smaller than that in the Java and Sumatra coasts (>4 °C), and higher than that in the eastern Indian Ocean and western Pacific Ocean warm pool regions (<1.5 °C). Inter-annual variability of SST over the region from model and observation is given in Fig. 4. SST anomalies are averaged over the domain 96.5°E–112°E and 4°S–16°N. The model could fairly well reproduce the inter-annually varying signals of SST over the region. The greatest discrepancy between the
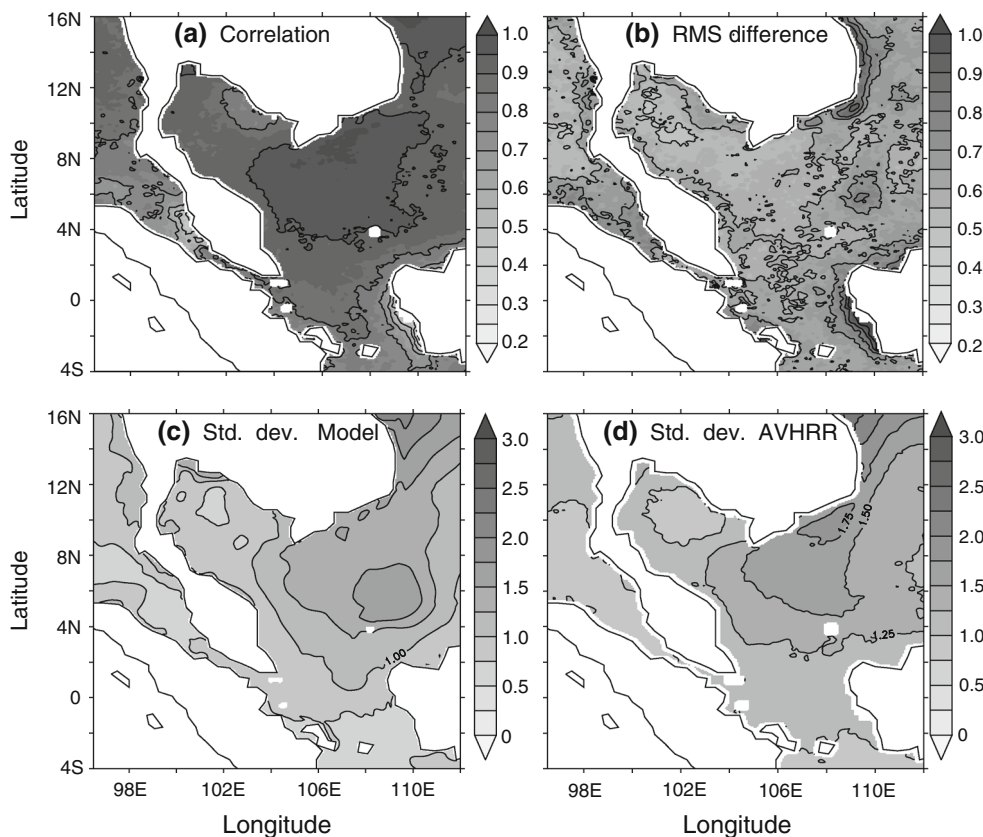

Fig. 3 **a** Correlation between the SST from the model and the AVHRR-Pathfinder observation. **b** RMS difference between SST from the model and the AVHRR-Pathfinder observation. **c** Model SST standard deviation. **d** AVHRR-Pathfinder SST standard deviation
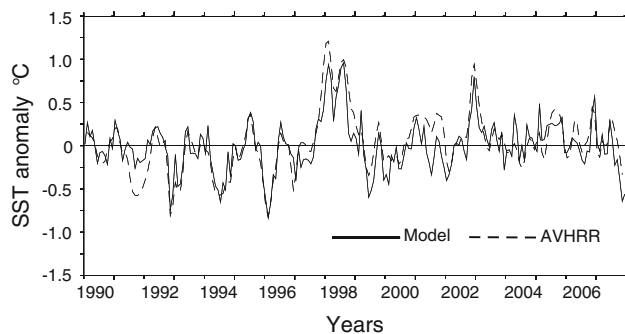
Fig. 4 SST anomaly from the model (*black line*) and AVHRR-Pathfinder observation (*dashed line*) over the SSCS. SST anomaly is averaged over the domain 96.5°E–112°E and 4°S–16°N

model and satellite observation is found during the years 1991 and 2001. The correlation and RMS difference between the model and observation are 0.84 and 0.18 °C, respectively.

3.2 Model sea surface height and surface circulation

Sea surface height in the SSCS exhibits strong seasonal signal associated with the southwest and northeast monsoons. Climatological evolution of the wind stress from ERA-interim and SSHA over the SSCS from the model and T/P satellite observation is shown in Fig. 5. The anticyclonic flow associated with the southwest monsoon induces Ekman convergence and a rise of the sea level between 104°E–112°E and 2°N–12°N. However, the northeast monsoon drags water from the deep SCS basin into the Sunda Shelf, eventually leading to an elevated sea level. In the SSCS, peak-to-peak amplitude in the seasonal variation of SSHA is largest over the Gulf of Thailand. SSHA varies from about −20 to +20 cm during the southwest to northeast monsoons. Another interesting feature of the sea level over the region is the reversal of sea level gradients between the SSCS and the Andaman Sea during the southwest and northeast monsoon periods.

The surface circulation pattern inferred by Wyrtki (1961) based on hydrographic observations, sea level records, and ship drifts is generally considered as a benchmark for understanding the SCS circulation. Model surface circulation climatology averaged for December–January (Fig. 6a) and June–July (Fig. 6b) is compared with the circulation pattern constructed by Wyrtki (1961; Plates 3a, 6a). In general, the model reproduces the main circulation features and shows good agreement with the reconstructions. Wyrtki (1961) pointed out that the surface current speeds of the Vietnam coastal current exceeds 1 m/s during the northeast monsoon. This feature is evident in the model simulation as well. As described in earlier studies (Wyrtki 1961; Dale 1956), cyclonic and

anticyclonic circulation patterns prevail in the SSCS during the northeast and southwest monsoons, respectively. Flow through the Malacca Strait is generally directed towards the Indian Ocean and it shows strong association to the surface gradient of the sea level between the SSCS and the Andaman Sea. In the Malacca Strait, the period of strongest flow is observed from January to April during the northeast monsoon (Fig. 6a) and mainly forced by the low sea level (Fig. 5) in the Andaman Sea (Wyrtki 1961). The volume transport through the Malacca Strait is smallest during the southwest monsoon period.

3.3 Mixed layer depth

The ocean upper mixed layer is considered as a region of homogeneous properties (viz. temperature, salinity, density, etc.) where active mixing occurs due to the surface wind stress, buoyancy fluxes or waves. The dynamic response of MLD to various atmosphere and ocean induced processes can substantially modify the SST. For instance, in the regions of strong upwelling when the MLD is shallow, significant surface temperature variations can occur than in places where MLD is deep (Qu et al. 1997). The thicker mixed layer has larger heat capacity and is, hence, less susceptible to external forcing. Though the MLD estimates are rather sensitive to the methodology employed for the analysis, the spatial distributions of MLDs show qualitatively consistent patterns in the world oceans (e.g., de Boyer Montégut et al. 2004). As defined in Sect. 2.1, a variable density criterion is used to compute the MLD. The time series of SST, MLD, and WKE averaged over the region 96.5°E–112°E and 4°S–16°N are plotted in Fig. 7. MLD in the SSCS has remarkable seasonal variation under the influence of monsoonal forcing. Generally, the MLD is deeper during June–August (summer) and December–February (winter), and shallow in March–May (spring) and September–October (fall). MLD over most of the SSCS does not exceed 40 m throughout the year (figure not shown). It should be noted that the depth of water over the Sunda sea-shelf is relatively shallow ($\sim$40 m) in the south, and gradually increases ($\sim$100 m) towards the central SCS. Moreover, due to its complex bathymetry, consisting of a number of narrow and shallow channels and islands, in a few instances the MLD reaches the bottom of the ocean. During the northeast monsoon (winter), MLD of about 35 m is seen in the Gulf of Thailand and offshore of southeast Vietnam (figure not shown).

In the northern parts of SCS, the annual cycle dominates in the SST and MLD (Qu 2001) while the SST has a clear semi-annual cycle in the SSCS (Fig. 7). In the warm phase, there is a gradual cooling of SST from May to August
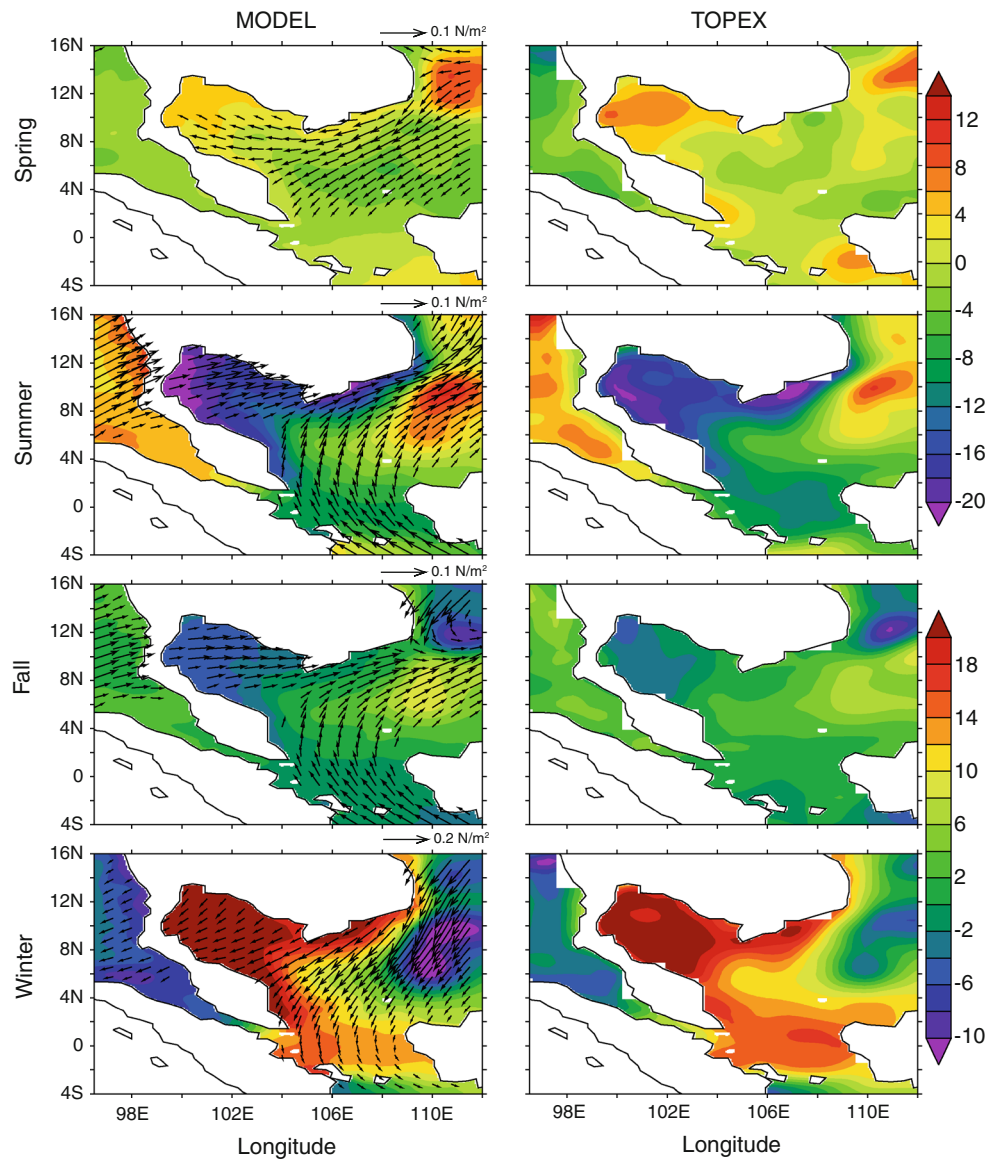
Fig. 5 Seasonal evolution of sea surface height anomaly (cm) over the SSCS. The seasons are referred w.r.t. the northern hemisphere: spring (March–May), summer (June–August), fall (September–November) and winter (December-February). The *left panel* represents the model and the *right panel* shows the Topex/Poseidon SSHA.

The color scale is different for the spring-summer and fall-winter seasons. The wind stress climatology from ERA-interim for respective seasons is shown as vectors in the *left panel*. Wind stress vectors above 0.02 N/m^2 are shown. Since the wind stress is relatively higher, the vector length is different during the winter

while slight warming is observed during September to October. Thereafter, relatively clear skies and weak winds aid the slender SST warming during the inter-monsoon period (September–October). With the onset of the northeast monsoon, the SST cools quickly from November till February. As the northeast monsoon withdraws from the region, surface temperature warms rapidly in February–April (pre-monsoon). An inverse relationship between the SST and MLD is well evident in the time series. Shallow MLD during the pre-monsoon and inter-monsoon accumulates the surface heat flux gained by the ocean into a thinner upper layer and warms up the ocean surface.

Deepening of the MLD imposed by the southwest or northeast monsoon winds eventually bring an end to the growth of heat flux in the upper ocean and subsequently a drop in the SST.

Following the monsoons, the WKE also exhibits a semi-annual distribution over the SSCS (Fig. 7). Similar to the MLD distribution, the WKE has a seasonal maximum in December–January and minimum during April. Though there can be local variations, the WKE explains the overall MLD variability over the SSCS. Inconsistency between these two variables is seen particularly during the months from July to August, where the MLD variation is not in
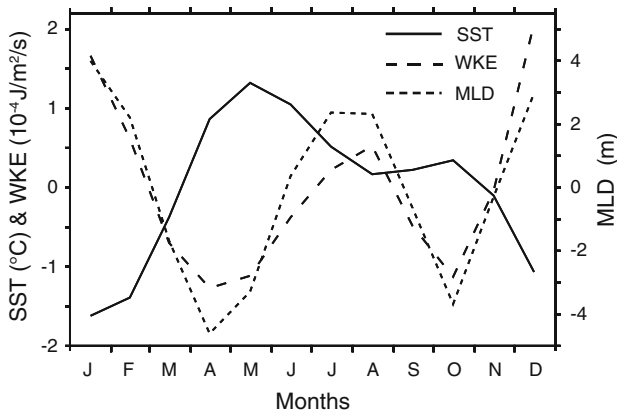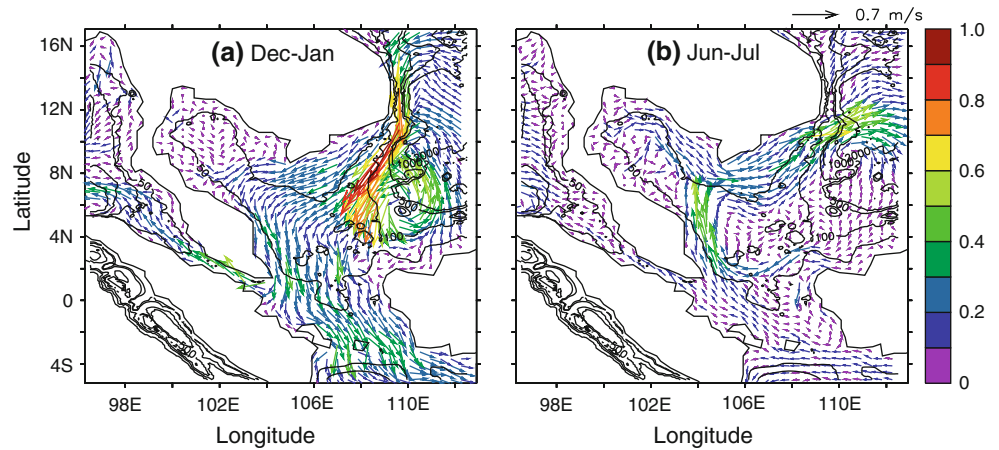
Fig. 7 SST (*black line*), wind kinetic energy (WKE) (*dashed line*), and MLD (*dotted line*) averaged over the region 96.5°E–112°E and 4°S–16°N. Annual mean value of 28.87 °C, 21 m, and 1.62 J/m²/s are removed from the SST, MLD, and WKE time series, respectively

phase with the WKE increase. This non-linearity suggests the possible role of ocean dynamics in driving the surface temperature, which will be explored through the mixed layer heat budget analysis in the following Section.

3.4 Mixed layer heat budget

The mixed layer temperature can be highlighted as a proxy for SST as well as to understand various physical processes contributing to the SST variations. Mixed layer heat budget analysis will be useful to make a quantitative assessment on the relative importance of different dynamical processes responsible for the SST variability. Seasonal evolution of the mixed layer temperature tendency averaged over the SSCS (99°E to 110.5°E, 2.5°S to 13.5°N) (refer Fig. 1) is shown in Fig. 8a. Since the relative contribution of horizontal diffusion is negligible, the term is omitted from the analysis. The sum of contributions from vertical heat advection and diffusion across the bottom of the mixed layer are treated as vertical processes in the analysis. As
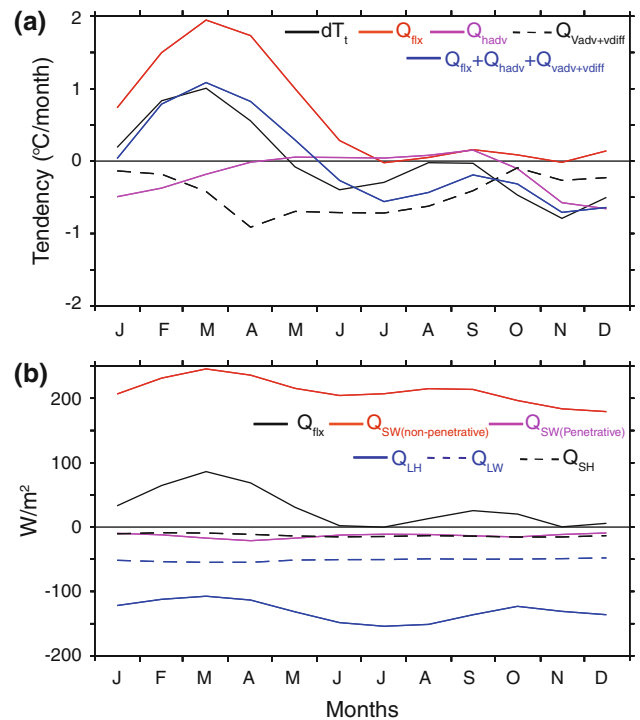

Fig. 8 a Upper panel shows the mixed layer heat budget climatology of the SSCS averaged over 99°E to 110.5°E, 2.5°S to 13.5°N. The total mixed layer temperature tendency (dT_t, *black line*), surface heat flux (Q_{flx}, *red line*), horizontal advection (Q_{hadv}, *purple line*), vertical ocean processes ($Q_{vadv+vdiff}$, *black dash*) and the sum of surface heat flux, horizontal advection, and vertical ocean processes (*blue line*) in °C/month are shown in the figure. **b** The net surface heat flux and individual flux contributions averaged over 99°E to 110.5°E, 2.5°S to 13.5°N are plotted in the *lower panel*. The net surface heat flux (Q_{flx}, *black line*), short wave flux absorbed in the mixed layer ($Q_{SW(non-penetrative)}$, *red line*), short wave flux penetrated below the mixed layer ($Q_{SW(penetrative)}$, *purple line*), latent heat flux (Q_{LH}, *blue line*), long wave flux (Q_{LW}, *blue dashed line*), and sensible heat flux (Q_{SH}, *black dashed line*) in W/m² are shown

shown in Fig. 7, the mixed layer temperature tendency also shows a semi-annual distribution under the influence of northeast and southwest monsoons.

The dominant process that determines the SSCS budget is the atmospheric forcing. Individual contributions of the short wave flux absorbed within the mixed layer (non-penetrative, red line), short wave flux reaching below the mixed layer (penetrative, purple line), latent heat flux (blue line), sensible heat flux (dashed black line), net long wave flux (dashed blue line) and net surface heat flux (black line) are shown in Fig. 8b. The non-penetrative component of shortwave flux is referred as the net short wave flux in the discussions. Net surface heat flux signifies an offsetting between the heating due to shortwave flux and cooling by latent heat and long wave fluxes. The seasonal shape of the net short wave flux is mainly determined by the seasonal march of the sun and the monsoons. During the northeast monsoon (winter season), the increased cloudiness and highest solar zenith angle results in the lowest short wave flux. Similarly, the cloudiness associated with the southwest monsoon (summer season) produces the secondary minimum in the short wave flux contribution. Seasonal cycle of the MLD is directly reflected in the heat loss due to the penetrative short wave flux. Deepened MLD during the southwest and northeast monsoon periods leads to the minima and shallow MLD in the pre-monsoon (March–April) and inter-monsoon (October) results in the maxima of heat loss due to the penetrative short wave radiation. The role of sensible heat flux is relatively small in the SSCS heat budget. Changes in the net long wave flux are very limited and it denotes heat loss from the ocean mixed layer of about 50 W/m^2 throughout the year. The magnitude of latent heat flux is roughly comparable with the net short wave flux. Seasonal cycle of latent heat flux is largely determined by the surface wind speed variations. It is obvious that the latent heat flux is higher during the monsoon periods when the winds are stronger over the region. Conversely, calm winds results in relatively low latent flux release from the ocean during the pre-monsoon and inter-monsoon periods. The increased shortwave flux and reduced latent heat flux induces positive primary and secondary maxima in the seasonal cycle of the SSCS net surface heat flux during the pre-monsoon and inter-monsoon periods. Meanwhile, the monsoonal processes are responsible for the relative minima in the net heat flux.

One remarkable feature of the SSCS mixed layer heat budget is the dominance of vertical ocean processes over the horizontal advection except during winter (Fig. 8a). Though weaker in magnitude, the horizontal heat advection tends to be positive during the southwest monsoon period. Meanwhile, horizontal advection has significant contribution to the total temperature variation during the northeast monsoon, where it accounts for the mixed layer temperature decrease by about 0.5 °C/month. The vertical ocean processes tend to cool the mixed layer temperature throughout the year and become significant during March–

September, where it imposes temperature change of −0.5 to −1 °C/month. Mixed layer temperature loss due to the vertical processes attains its maximum in April coinciding with the shallowest MLD over this region (Fig. 7). From January to April, weakening of the northeast monsoon results in rapid shoaling of the MLD (Fig. 7) and reduction in heat loss due to the horizontal advection (Fig. 8a). The cooling effect due to the detrainment and vertical diffusion gradually increases during this period and together with the decrease of surface heat flux leads to negative temperature tendency by April. The vertical processes have a significant role in the temperature cooling during summer. Most of the SSCS experiences loss of heat by vertical processes during April, which is mainly contributed by the vertical diffusion. From warm mixed layer, the exchange of heat to subsurface takes place through diffusive processes during the pre-monsoon period, whereas the vertical diffusion together with the cold water entrainment (upwelling) off the eastern side of the Peninsular Malaysia and eastern coasts of Vietnam contribute to the heat loss during the southwest monsoon period. As the southwest monsoon diminishes by late summer, the vertical advective/diffusive fluxes also become weak. Meanwhile, the positive contributions from horizontal advection and surface heat fluxes tend to warm the mixed layer during the inter-monsoon period. With the onset of the northeast monsoon, the horizontal advective flux increases and contributes significantly to the temperature cooling. Strong northeast monsoon currents (Fig. 6a) bring cold water from the northern SCS to the south. To the SSCS, the cold water advection occurs through the northern and northeastern boundary. The horizontal advective processes are prominent off the southeastern and eastern regions of Vietnam during this season. Impact of vertical processes during this period is relatively smaller than the horizontal fluxes, typically by a factor of 2.

The MLD heat budget is not exactly closed in our analysis and the imbalance is significant during April–May and July–September. In spite of this discrepancy, the encouraging fact is that the sum of net surface heat flux and oceanic processes along with the MLD temperature tendency exhibit identical seasonal patterns. The differences mainly appear due to the errors in the numerical schemes and approximations employed in the analysis.

Though there is no explicit SST relaxation in the model, specifying the air temperature and specific humidity at 2-m can strongly constrain the model SST to remain close to the observation. In reality, the underlying ocean surface temperature primarily determines the changes in the air temperature and humidity. By specifying these parameters the computed surface fluxes will try to restore the model SST towards the observation. Consequently, the air-sea fluxes computed with the *bulk formulae,* using the model SST, tend to compensate the error/missing processes in the

model simulation by introducing a flux anomaly (de Boyer Montégut et al. 2007). These flux anomalies will be larger when the difference between the model and observed SSTs are higher. The heat budget term corresponding to this 'hidden relaxation term' is not accounted in our analysis. Hence, a qualitative description is presented during the analysis of inter-annual heat budget anomalies in Sect. 3.5.

The heat budget analysis of the mixed layer illustrates that the surface heat flux is one of the dominant factors that determines the seasonal cycle of mixed layer temperature in the SSCS. Mixed layer temperature tendency in the SSCS evolves almost in phase with the surface heat flux variation. Significant phase difference between these two factors is observed during the southwest monsoon when the vertical ocean processes primarily control the temperature tendency. The role of horizontal advection becomes important from late summer through winter. In general, the budget analysis demonstrates a net balance between the vertical processes and surface heat flux during the pre-monsoon and southwest monsoon, and between surface heat and horizontal and vertical ocean processes in the northeast monsoon.

3.5 Inter-annual variability of the SSCS mixed layer temperature

The inter-annual variability of the SSCS mixed layer temperature and heat content is examined in this Section. Due to its geographic location in the middle of the Indo-Pacific warm pool, the climate variability in the SCS is significantly modulated by the air-sea coupled phenomenas over the Pacific and Indian Oceans (e.g., ENSO, IOD, etc.). EOF analysis of the mixed layer temperature and heat content anomalies from 1991 to 2007 has been performed to evaluate the dominant modes of variability. The linear trend has been removed before doing the analysis. The first and second dominant modes of variability of the mixed layer temperature and heat content anomalies are shown in Fig. 9. The first and second dominant modes of the mixed layer temperature explain 60 and 8 % of the total variability in the SSCS; the variability explained by the first and second modes of the mixed layer heat content are 28 and 10 %, respectively. Though their spatial distributions are not quite similar, the EOF1 of mixed layer temperature and heat content show uniform loading over the SSCS (Fig. 9a and c). Peak amplitude of the heat content variability is seen in the Gulf of Thailand and center portions of the Sunda sea-shelf. The Time Coefficient Functions of the first EOF mode (TCF1) of temperature and heat content are significantly linked to the Nino3.4 index (Fig. 10a and b). The correlation coefficients between the TCF1 of the mixed layer temperature and heat content with the Nino3.4 index are 0.34 and 0.33, respectively, indicating significance level above 99 %. Linear lag-correlation analysis

indicates that TCF1s are best correlated with ENSO when the TCF1 lags the Nino3.4 index by 5 months. The correlation increases to 0.67 and 0.55, respectively, for the mixed layer temperature and heat content with a lag of 5 months. The SSCS mixed layer temperature anomalies related to the ENSO peak in the following boreal spring season (March–April). Second dominant mode of variability in the SSCS mixed layer temperature (heat content) anomaly is distinguished by a meridional dipole structure (Fig. 9b and d), which explains 8 (10 %) of the total variability. The amplitude of variability has roughly equal strength in the positive and negative loading centers.

The ocean dynamical processes associated with the inter-annual mixed layer temperature anomalies are investigated through the heat budget analysis. Monthly mean anomalies of heat budget terms averaged over the region 99°E to 110.5°E and 2.5°S to 13.5°N expressed as regression with respect to the mixed layer temperature tendency is shown in Fig. 10c. Corresponding regression coefficients of the net surface heat flux, vertical ocean processes, and horizontal advection are 1.1, −0.35 and 0.17, respectively. These three terms explain about 92 % of the total temperature change. The surface heat flux represents the dominant process in driving the inter-annual mixed layer temperature variability in the SSCS. Negative contribution by the vertical ocean processes indicates that it acts opposite to the mixed layer temperature change. The contribution from horizontal advection is relatively small though not negligible. Strong positive mixed layer temperature anomalies are seen after the El Nino events (e.g., 1991–1992, 1994–1995 and 1997–1998). The mixed layer warming is primarily attributed to the positive surface heat flux anomalies. The increased shortwave radiation due to clear skies and reduced latent heat loss because of calm winds are the main contributors to the net heat flux anomalies. Meanwhile, the shallow mixed layer increases the heat loss to the subsurface by the diffusive and detrainment processes. The horizontal advective processes tend to aid the warming marginally during the El Nino events.

The SCS exhibits a basin-wide warming (cooling) following the El Nino (La Nina) events. SST anomalies in the tropical Pacific Ocean modify the atmospheric circulation and hence induce significant changes to the air-sea fluxes over the SCS (Klein et al. 1999; Fang et al. 2006). Upper ocean warming in the SCS during the El Nino years is largely associated with the weakened northeast monsoons (Fang et al. 2006). Clear skies as well as dry and calm winds due to the diminished northeast monsoon have led to the warming of the ocean's surface following the El Nino events. In particular, the strong mixed layer heating during the El Nino events in 1994–1995 and 1997–1998, and cooling in the 1998–1999 La Nina event, are well evident in the model simulations (Fig. 10a and b).

Fig. 9 *Upper panel* shows the spatial distribution of the mixed layer temperature variability corresponding to the first (**a**) and second (**b**) EOF modes in the SSCS. Similarly, first (**c**) and second (**d**) dominant modes of the mixed layer heat content variability are shown in the *lower panels*. The variability explained by these modes is also given. The *thick black line* represents the zero contours
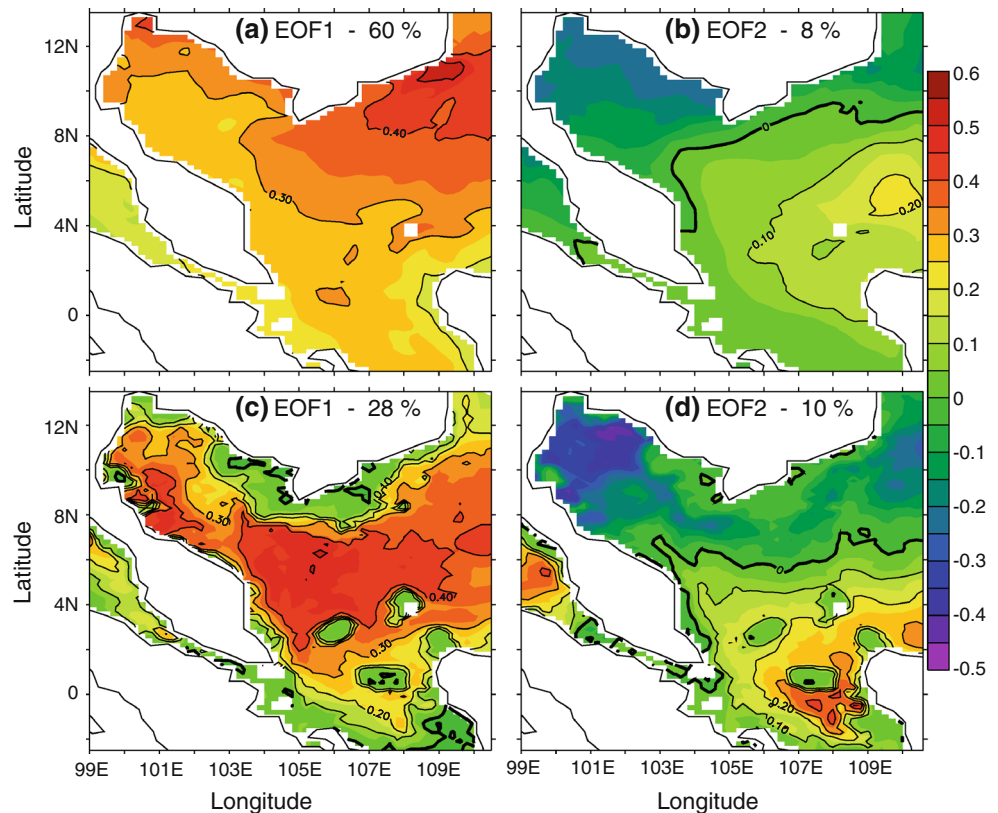

The role of remote forcing on the mixed layer temperature anomalies associated with the ENSO events is addressed by estimating the lateral heat transport into the SSCS region. Figure 11 shows the mixed layer heat transport anomalies through the lateral boundaries to the SSCS domain 99°E to 110.5°E and 2.5°S to 13.5°N. The sum of heat transport anomaly through the eastern (110.5°E) and northern (13.5°N) boundaries is plotted as HTA$_{East}$ in the figure. HTA$_{south}$ and HTA$_{west}$ denote the heat transport anomalies through the Karimata Strait (2.5°S) and western entrance of the Malacca Strait (99°E), respectively. Here, the positive anomaly indicates a net gain of heat into the SSCS and vice versa. In general, following the El Nino events; positive heat transport anomalies appear at the eastern boundary. For instance, the positive heat transport peaks during 1992, 1995, 1998, 2004 and 2006–2007. Indeed, the El Nino events enforce a weakening of the northeast monsoon winds over the SCS. A diminished northeast monsoon weakens the prevailing cyclonic circulation in the SCS. Consequently, the southward advection of cold water from the northern SCS either collapses or decreases, which can lead to positive heat transport anomalies. Conversely, there is a net heat transport loss during the La Nina events in 1998–1999 and 1999–2000, which implies the strengthening of the northeast monsoon currents and increased southward advection of cold water. Though 2004 was a weak El Nino year, a

sharp peak in the heat transport anomaly (HTA$_{East}$) is observed. In contrast to the strong El Nino events, the heat transport anomalies peak by the end of the year and decay abruptly in the beginning of 2005. Compensating the heat gain/heat loss through the eastern boundary, heat transport through the Karimata Strait exhibits negative/positive anomalies. The role of heat transport through the Malacca Strait is relatively weak compared to the transport anomalies through the eastern and southern boundaries. Considerable heat transport anomalies are seen during the El Nino events in 1997–1998 and 2004.

4 Discussions and conclusion

The seasonal and inter-annual variability of the mixed layer temperature in the SSCS is investigated in this study. Scarcity of observations and relatively coarse resolution of the numerical ocean models have imposed certain limitations in studying the thermodynamical characteristics of the SSCS. The simulations from a 3-dimensional, eddy-resolving, sigma-coordinate regional ocean general circulation model forced by ocean and atmosphere re-analysis datasets from ERA-interim and SODA has been employed for the analysis. As a first step, the model simulated SST and SSHA are compared with the satellite observations from AVHRR-pathfinder and Topex/Poseidon altimeter.

Fig. 10 a The time coefficient of first EOF mode (TCF1) of mixed layer temperature variability (*black line*) overlaid with the Nino3.4 index (*red line*). **b** The time coefficient of first EOF mode (TCF1) of mixed layer heat content variability (*black line*) overlaid with the Nino3.4 index (*red line*). **c** Anomalies of mixed layer heat budget anomalies (°C/month) averaged over the region 99°E to 110.5°E, 2.5°S to 13.5°N expressed as regression w.r.t. mixed layer temperature tendency. Mixed layer temperature tendency (dT_t, *black line*), surface heat flux (Q_{flx}, *red line*), vertical ocean processes ($Q_{vertical}$, *blue line*), and horizontal advection (Q_{hadv}, *purple line*) are plotted

(a) Mixed layer temperature EOF

(b) Mixed layer heat content EOF

(c) Mixed layer heat budget anomaly
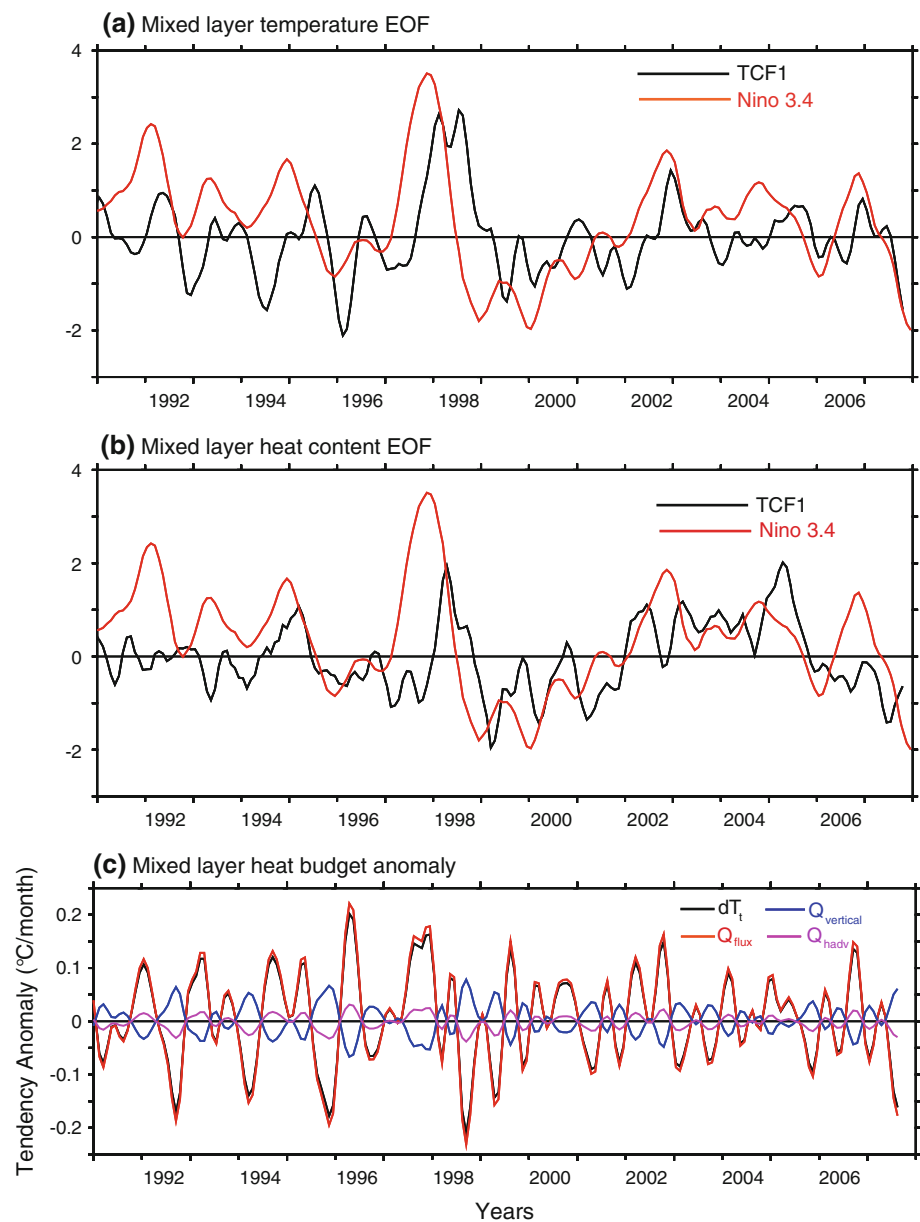
Seasonal and inter-annual evolutions of the SST, SSHA, and surface circulation in the SSCS are well reproduced by the model and show good qualitative as well as quantitative agreement with the observations.

MLD in the SSCS is relatively shallow and rarely exceeds depths above 40 m. Strong seasonal signal is observed with deeper MLDs during the northeast and southwest monsoons and shallow MLDs during the pre- and inter-monsoons. Deepest MLDs are encountered in the Gulf of Thailand and south off Vietnam during the northeast monsoon period. Seasonally varying monsoon wind is primarily responsible for the MLD variations in the SSCS. The wind-induced stirring explains most of the seasonal MLD variability over the region.

The surface heat flux is one of the dominant factors that determine the seasonal evolution of the SSCS mixed layer temperature. In the mixed layer thermodynamics, the vertical ocean processes plays a significant role in determining the upper ocean temperature tendency, especially during the pre-monsoon and southwest monsoon periods. The vertical advection and diffusive processes act as effective cooling mechanism on these periods. In the vertical ocean processes, entrainment of cold water into the mixed layer dominates in the southwest monsoon. Meanwhile, the vertical diffusion of temperature from the upper ocean prevails during the pre-monsoon warming phase when the MLD is relatively shallow. Onset of the northeast monsoon triggers strong slope current along the Vietnam coast
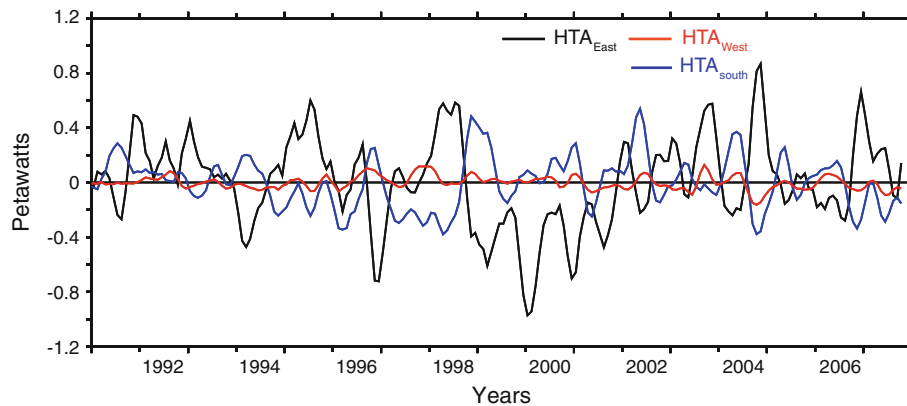
Fig. 11 Mixed layer heat transport anomaly through the lateral boundaries to the SSCS domain (99°E to 110.5°E and 2.5°S to 13.5°N). The sum of heat transport anomaly through the eastern (110.5°E) and northern (13.5°N) boundaries are plotted as HTA$_{East}$ (*black line*). HTA$_{south}$ (*blue line*) and HTA$_{west}$ (*red line*) represent the heat transport anomalies through the Karimata Strait (2.5°S) and western entrance of the Malacca Strait (99°E), respectively. Positive anomalies indicate net heat transport into the control volume. The time series are smoothed using 5-month sparzen smoother

resulting in the southward advection cold water to the SSCS. The horizontal advection contributes significantly to the rapid SST cooling during the winter monsoon. In summary, the SSCS mixed layer heat budget demonstrates a net balance between the surface heat flux and vertical ocean processes from spring to fall, and a balance between the surface heat flux, horizontal advection, and vertical ocean processes in the winter.

First dominant EOF mode of the mixed layer temperature anomaly is characterized by a basin-wide warming/cooling in the SSCS that explains 60 % of the total variability. Corresponding time coefficient function shows significant correlation with the Nino3.4 index and is best correlated (0.67) with a lag of 5 months. EOF1 of the model mixed layer heat content anomalies also denote a uniform warming/cooling over the SSCS (explains 28 % of the total variability). However, their spatial distributions of the amplitude of variability are slightly different. The surface heat flux represents the dominant process in driving the inter-annual mixed layer temperature variability in the SSCS. A diminished northeast monsoon during the El Nino events weakens the cyclonic circulation in the SCS. Consequently, this will lead to a reduction of southward advection of cold water by the western boundary current along the Vietnam coast and warming of the mixed layer in the SSCS. Conversely, La Nina events enhance the cyclonic circulation and thereby negative heat transport (cold water transport) to the SSCS.

As a final comment, the study suggests that although the ENSO remains a dominant mechanism in driving the upper ocean climate variability in the SSCS, the mixed layer heat content variability explained by the ENSO related first mode almost reduces by a factor of 2 when compared with the ENSO influence on the mixed layer temperature/SST

variability. This result is consistent with the notion that the inter-annual variability of SST is quite different from that of the upper ocean heat content/integrated seawater temperature below the sea surface in the SCS (e.g., Fang et al. 2006). The role of other tropical air-sea interaction phenomena, such as the Indian Ocean Dipole, may also become prominent in the mixed layer heat content variability. The correlations of September–October–November Dipole Mode Index (representing the intensity of IOD events) and November–December–January Nino3.4 index with the TCF2 of mixed layer heat content are 0.51 and 0.50, respectively. Since TCF2 is significantly correlated with the IOD and ENSO, the traditional linear correlation analysis will not be sufficient to resolve their relative influences. Further, detailed analysis (e.g., partial correlation) using multi-decadal datasets needs to be performed for isolating the variations induced by the ENSO and IOD on SSCS upper ocean heat content. Also, it should be noted that the first two dominant modes of mixed layer heat content anomaly explains only about 38 % of the total variability. This suggests that a larger fraction (62 %) of the heat content variability is related to various other processes which are not considered in this study.

The harmful algal blooms (HAB)/red tides are of great concern due to the economic loss and its impact on human health. The socio-economic profile of the Southeast Asian region largely depends on various onshore as well as offshore activities including fisheries and utilization of other natural resources. HAB occur frequently in the SCS and cause enormous loss to the coastal fisheries (Leong et al. 2012; Wang et al. 2008). The air-sea parameters including the wind, solar radiation, ocean currents, and upper ocean temperature are important factors influencing the HAB. Wang et al. (2008) suggested that the anomalous HAB events in the SCS during 1998 might be linked to the

1997–1998 El Nino conditions. Associated with the mixed layer temperature and circulation changes, the possible relationship between the climate phenomena and HAB over this region needs to be explored further.

References

Alexander MA, Bladé I, Newman M, Lanzante JR, Lau N-C, Scott JD (2002) The atmospheric bridge: the influence of ENSO teleconnections on air–sea interaction over the global Oceans. J Clim 15:2205–2231

Cai RS, Chen JL, Tan HJ (2011) Variations of the sea surface temperature in the offshore area of China and their relationship with the East Asian monsoon under the global warming. Clim Environ Res 16(1):94–104 (in Chinese with English abstract)

Carton JA, Giese BS (2008) A reanalysis of ocean climate using Simple Ocean Data Assimilation (SODA). Mon Wea Rev 136:2999–3017

Chao CY, Shaw PT, Wu SY (1996) El Nino modulation of the South China Sea circulation. Prog Oceanogr 38:51–93

Chu PC, Lu S, Chen Y (1997) Temporal and spatial variabilities of the South China Sea surface temperature anomaly. J Geophys Res 102:20,937–20,955

Chu PC, Edmons NL, Fan CW (1999) Dynamical mechanisms for the South China Sea seasonal circulation and thermohaline variabilities. J Phys Oceanogr 29:2971–2989

Cushman-Roisin B (1981) Deepening of the wind-mixed layer: a model of the vertical structure. Tellus 33:564–582

Dale WL (1956) Wind and drift current in the South China Sea. Malayan J Trop Geogr 8:1–31

de Boyer Montégut C, Madec G, Fischer AS, Lazar A, Iudicone D (2004) Mixed layer depth over the global ocean: an examination of profile data and a profile-based climatology. J Geophys Res 109:2003. doi:10.1029/2004JC002378

de Boyer Montégut C, Vialard J, Shenoi SSC, Shankar D, Durand F, Ethé C, Madec G (2007) Simulated seasonal and interannual variability of mixed layer heat budget in the northern Indian Ocean. J Clim 20:3249–3268

Debreu L, Marchesiello P, Penven P, Cambon G (2012) Two-way nesting in split-explicit ocean models: algorithms, implementation and validation. Ocean Model 49–50:1–21

Dee DP et al (2011) The ERA-Interim reanalysis: configuration and performance of the data assimilation system. Q J R Meteorol Soc 137:553–597. doi:10.1002/qj.828

Fairall CW, Bradley EF, Rogers DP, Edson JB, Young GS (1996) Bulk parameterization of air-sea fluxes for tropical Ocean-Global atmosphere Coupled-Ocean atmosphere response experiment. J Geophys Res 101(C2):3747–3764. doi:10.1029/95JC03205

Fang G, Susanto D, Soesilo I, Zheng Q, Qiao F, Wei Z (2005) A note on the South China Sea shallow interocean circulation. Adv Atmos Sci 22(6):946–954. doi:10.1007/BF02918693

Fang G, Chen H, Wei Z, Wang Y, Wang X, Li C (2006) Trends and interannual variability of the South China Sea surface winds, surface height, and surface temperature in the recent decade. J Geophys Res 111:C11S16. doi:10.1029/2005JC003276

Grodsky SA, Carton JA, Liu H (2008) Comparison of bulk sea surface and mixed layer temperatures. J Geophys Res 113:C10026. doi:10.1029/2008JC004871

Ho C-R, Zheng Q, Soong YS, Kuo N-J, Hu JH (2000) Seasonal variability of sea surface height in the South China Sea observed with TOPEX/Poseidon altimeter data. J Geophys Res 105(C6):13981–13990. doi:10.1029/2000JC900001

Jerlov NG (1968) Optical Oceanography. Elsevier, pp 194

Kienast M, Steinke S, Stattegger K, Calvert SE (2001) Synchronous tropical South China Sea SST change and greenland warming during deglaciation. Science 291:2132. doi:10.1126/science.1057131

Kim S-B, Fukumori I, Lee T (2006) The closure of the ocean mixed layer temperature budget using level-coordinate model fields. J Atmos Oceanic Technol 23:840–853

Klein SA, Soden BJ, Lau N-C (1999) Remote sea surface variations during ENSO: evidence for a tropical atmospheric bridge. J Clim 12(4):917–932

Large WG, McWilliams JC, Doney SC (1994) Oceanic vertical mixing: a review and a model with a nonlocal boundary layer parameterization. Rev Geophys 32:363–403

Lau N-C, Nath MJ (1996) The role of the "atmospheric bridge" in linking tropical Pacific ENSO events to extratropical SST anomalies. J Clim 9:2036–2057

Lemarié F, Kurian J, Shchepetkin A, Molemaker MJ, Colas F, McWilliams JC (2012) Are there inescapable issues prohibiting the use of terrain-following coordinates in climate models? Ocean Model 42:57–79

Leong SCY, Tkalich P, Patrikalakis NM (2012) Monitoring harmful algal blooms in Singapore: developing a HABs observing system. OCEANS 2012-Yeosu. doi:10.1109/OCEANS-Yeosu.2012.6263428

Li L, Xu JD, Cai RS (2002) Trends of sea level rise in the South China Sea during 1990s: an altimetry result. Chin Sci Bull 47(7):582–585

Liu Q, Jiang X, Xie S-P, Liu WT (2004) A gap in the Indo-Pacific warm pool over the South China Sea in boreal winter: seasonal development and interannual variability. J Geophys Res 109:C07012. doi:10.1029/2003JC002179

Liu C, Du Y, Zhang Q, Chen T, Wang D (2007) Responses of oceans to global warming and observation evidence in the South China Sea. Adv Clim Change Res 3(1):8–13 (in Chinese with English abstract)

Liu Q, Kaneko A, Su J (2008) Recent progress in studies of the South China Sea circulation. J Oceanogr 64:753–762

Liu Y, Peng ZC, Wei GJ, Chen TG, Sun WD, He JF, Sun RY, Liu GJ (2009) Variation of summer coastal upwelling at northern South China Sea during the last 100 years. Geochimica 38(4):317–322 (in Chinese with English abstract)

Liu Q, Feng M, Wang D (2011) ENSO-induced interannual variability in the southeastern South China Sea. J Oceanogr 67:127–133

Marchesiello P, McWilliams JC, Shchepetkin A (2001) Open boundary conditions for long-term integration of regional oceanic models. Ocean Model 3:1–20

Marchesiello P, Debreu L, Couvelard X (2009) Spurious diapycnal mixing in terrain-following coordinate models: the problem and a solution. Ocean Model 26:156–169

Niiler PP (1975) Deepening of the wind-mixed layer. J Mar Res 33:405–422

Ose T, Song Y, Kitoh A (1997) Sea surface temperature in the South China Sea: an index for the Asian monsoon and ENSO system. J Meteor Soc Japan 75:1091–1107

Penven P, Debreu L, Marchesiello P, McWilliams JC (2006) Evaluation and application of the ROMS 1-way embedding

procedure to the central California upwelling system. Ocean Model 12:157–187

Pickard GL, Emery WJ (1990) Descriptive physical Oceanography, 5th edn. Butterworth, London, p 320

Qu T (2000) Upper layer circulation in the South China Sea. J Phys Oceanogr 30:1450–1460

Qu T (2001) Role of ocean dynamics in determining the mean seasonal cycle of the South China Sea surface temperature. J Geophys Res 106:6943–6955

Qu T, Meyers G, Godfrey JS, Hu D (1997) Upper ocean dynamics and its role in maintaining the annual mean western Pacific warm pool in a global GCM. Int J Climatol 17:711–724

Qu T, Kim YY, Yaremchuk M, Tozuka T, Ishida A, Yamagata T (2004) Can luzon strait transport play a role in conveying the impact of enso to the south china sea? J Clim 17:3644–3657

Qu T, Du Y, Strachan J, Meyers G, Slingo J (2005) Sea surface temperature and its variability in the Indonesian region. Ocean-ography 18(4):50–61

Rong Z, Liu Y, Zong H, Cheng Y (2007) Interannual sea level variability in the South China Sea and its response to ENSO. Global Planet Change 55:257–272

Saji NH, Yamagata T (2003) Possible impacts of Indian Ocean dipole mode events on global climate. Clim Res 25(2):151–169

Saji NH, Goswami BN, Vinayachandran PN, Yamagata T (1999) A dipole mode in the tropical Indian Ocean. Nature 401:360–363

Shchepetkin A, McWilliams JC (1998) Quasi-monotone advection schemes based on explicit locally adaptive dissipation. Mon Wea Rev 126:1541–1580

Tomita T, Yasunari T (1996) Role of the northeast winter monsoon on the biennial oscillation of the ENSO/monsoon system. J Meteorol Soc Japan 74:399–413

Vialard J, Delecluse P (1998) An OGCM study for the TOGA decade. Part I: role of salinity in the physics of the Western Pacific fresh pool. J Phys Oceanogr 28:1071–1088

Vialard J, Menkes C, Boulanger J-P, Delecluse P, Guilyardi E, McPhaden MJ, Madec G (2001) A model study of Oceanic mechanisms affecting equatorial Pacific Sea surface temperature during the 1997–98 El Niño. J Phys Oceanogr 31:1649–1675

Wang B, Wu R, Fu X (2000) Pacific–East Asian teleconnection: how does ENSO affect East Asian climate? J Clim 13:1517–1536

Wang D, Xie Q, Du Y, Wang W-Q, Chen J (2002) The 1997–1998 warm event in the South China Sea. Chin Sci Bull 47:1221–1227

Wang Y, Fang G, Wei Z, Qiao F, Chen H (2006a) Interannual variation of the South China Sea circulation and its relation to El Nino, as seen from a variable grid global ocean model. J Geophys Res. doi:10.1029/2005JC003269

Wang C, Wang W, Wang D, Wang Q (2006b) Interannual variability of the South China Sea associated with El Niño. J Geophys Res 111:C03023. doi:10.1029/2005JC003333

Wang SF, Tang DL, He FL, Fakuyo Y, Azanza RV (2008) Occurrences of harmful algal blooms (HABs) associated with ocean environments in the South China Sea. Hydrobiologia 596(1):79–93

Webster PJ, Moore AM, Loschnigg JP, Leben RR (1999) Coupled ocean-atmosphere dynamics in the Indian Ocean during 1997–98. Nature 401:356–360

Wu C-R, Shaw P-T, Chao S-Y (1998) Seasonal and interannual variations in the velocity field of the South China Sea. J Oceanogr 54:361–372

Wyrtki K (1961) Physical oceanography of Southeast Asian waters, NAGA report. In: Scientific results of marine investigations of the South China Sea and Gulf of Thailand. Scripps Institution of Oceanography. La Jolla, California, pp 2–195

Xie SP, Xie Q, Wang DX, Liu WT (2003) Summer upwelling in the South China Sea and its role in regional climate variations. J Geophys Res 108(C8):3261. doi:10.1029/2003JC001867

Yang H, Wu L (2012) Trends of upper-layer circulation in the South China Sea during 1959–2008. J Geophys Res 117:C08037. doi:10.1029/2012JC008068

Yuan Y, Yang H, Zhou W, Li C (2008) Influences of the Indian Ocean dipole on the Asian summer monsoon in the following year. Int J Climatol 28:1849–1859